
GENERATING VARIOUS AIRFOIL SHAPES WITH REQUIRED LIFT COEFFICIENT USING CONDITIONAL VARIATIONAL AUTOENCODERS

A PREPRINT

Kazuo Yonekura*

Department of Systems Innovation
The University of Tokyo
Tokyo, JAPAN 113-8656

Kazunari Wada

Department of Systems Innovation
The University of Tokyo
Tokyo, JAPAN 113-8656

Katsuyuki Suzuki

Department of Systems Innovation
The University of Tokyo
Tokyo, JAPAN 113-8656

June 21, 2021

ABSTRACT

Multiple shapes must be obtained in the mechanical design process to satisfy the required design specifications. The inverse design problem has been analyzed in previous studies to obtain such shapes. However, finding multiple shapes in a short computation period is difficult while using the conventional methods. This paper proposes the use of the conditional variational autoencoders (CVAE) with normal distribution, denoted by \mathcal{N} -CVAE, along with the von Mises-Fischer distribution, denoted by \mathcal{S} -CVAE, to find multiple solutions for the inverse design problems. Both the CVAE models embed shapes into a latent space. The \mathcal{S} -CVAE enables the separation of data in the latent space, whereas the \mathcal{N} -CVAE embeds the data in a narrow space. These different features are used for various tasks in this study. In one of the tasks, the dataset consists of only one type of data and generates similar airfoils. Here, \mathcal{S} -CVAE outperforms \mathcal{N} -CVAE because it can separate the data. Another task involves combining different types of airfoils and generating new types of data. \mathcal{N} -CVAE is useful in this instance since it embeds different shapes in the same latent area, due to which, the model outputs intermediate shapes of different types. The shape-generation capability of \mathcal{S} -CVAE and \mathcal{N} -CVAE are experimentally compared in this study.

Keywords Design exploration · Inverse problem · Variational autoencoder · Airfoil design

1 Introduction

A mechanical design must primarily satisfy the given design specifications. The mechanical design process can be divided into two phases: rough design and tuning. In the rough design process, rough drawings are produced by human designers, often considering trade-off relationships. One candidate is then chosen and the process of tuning the shape is initiated. The rough design process incurs a large amount of labor cost, and the result depends on the experience of the designer. A candidate shape must be obtained in a short period of time. This task is known as an inverse design problem.

Inverse analysis and design have gained considerable attention in the recent years for application in fluid machinery such as turbines, pumps, and wings [1, 2, 3, 4, 5]. The numerical sensitivity analysis is one of the methods of inverse design

*yonekura@struct.t.u-tokyo.ac.jp

[6, 7]. However, the sensitivity-based methods require a long computation time. The principal component analysis (PCA) method requires less computation time and can be categorized as a data-driven approach. The PCA-based dimension reduction approach is used for design exploration in fields such as aerospace [8] and marine engineering [9]. Bui-Thanh et al. [10] also utilized the PCA method for the inverse design of flow fields. Lee et al. [11] utilized a dimension-reduction method for reliability analysis and optimization. This method analyzes and extracts the features from various shapes and designs. However, it is difficult to consider the correlations such as the airfoil shape and the lift coefficient, between the shape features and the aerodynamic performance. A performance-driven design was therefore proposed in the architecture [12] to consider the correlations between the performance and the design parameters. However, the methods mentioned above do not provide an exact design which satisfies the specifications, due to which, multiple designs must be explored based on the additional analyses. Therefore, the shapes which satisfy the specified requirements must be directly obtained.

A new type of shape can be obtained by using the PCA-based methods even though machine learning generally performs the interpolation of data. Nita et al. [13] constructed a dataset with different shapes and generated a low-dimensional linear space by applying the PCA method to the dataset. A new type of shape [14] was then obtained from the linear space. In this example, the dataset consists of different types of data located far away from each other in the design space. The new type of data is located between these data. It is essentially a combination of different types of data. It is desirable to obtain novel shapes from an application point of view, due to which, the design methods must be capable of handling multiple types of data.

The use of deep neural networks to generate shapes from data has gained interest in the recent years. [15] proposed the generative adversarial network (GAN) model to generate shapes with low or high lift coefficient. [16] proposed the BézierGAN to obtain smooth airfoils. [?] proposed the conditional variational autoencoder (CVAE) to output smooth shapes with specific lift coefficient. However, the variations in the generated shapes and the combination of different types of airfoils have not been analyzed in the previous studies. In this study, two types of CVAE models have been used to generate various types of airfoil shapes. The first is a CVAE model with a normal distribution of \mathcal{N} -CVAE, which is an ordinal CVAE model. The other is a CVAE model with a von Mises-Fischer (vMF) distribution, which is called \mathcal{S} -CVAE.

In the recent years, machine learning, particularly deep learning, has considerably improved in various fields, such as image recognition and signal processing. The capability of the feature extraction methods have also been improved based on deep learning. Deep neural network has applied to mechanical design in several studies [17, 18, 19, 20, 21]. One of the deep neural network models is the autoencoder (AE), which is a dimension reduction method, and has been successfully used for image processing [22]. An AE and a variational AE (VAE) [23] are composed of neural networks; they extract the features from the input data and represent the data as small-dimensional latent vectors. The VAEs are used in various fields, such as image processing [24] and anomaly detection [25]. A conditional VAE [26] adds nodes to the VAE architecture used to feed the labels with input; the CVAE extracts the features while considering the labels. The VAEs and the CVAEs are referred to as generative models because they generate new data and images that do not exist in the real world. These generative models are mainly studied in computer science and are used for image processing [27].

The ordinal VAE model has been observed to produce the same result even if the latent variables are different. This issue is called the posterior collapse or the Kullback-Leibler (KL) collapse. [28, 29] proposed a hyperspherical VAE (\mathcal{S} -VAE) to resolve the KL collapse issue. \mathcal{S} -VAE uses a von Mises-Fisher distribution rather than a normal distribution in the latent space.

The proposed method can be used by a designer to compare the airfoils with different specifications but with the same loss coefficient to obtain a rough idea of the design or to consider the trade-off relationships. Generally, a considerable amount of effort is required to design each shape. This issue can be resolved by using the CVAE; the designers can also produce different shapes in a short period of time with this method. The designers require a wide variety of shapes to consider the trade-off relationships. Additionally, novel shapes which are different from the training dataset are required to obtain a novel concept of a product.

Two design tasks are discussed in this paper. Firstly, a single type of airfoil dataset, called the NACA airfoil is used, and a wide variety of shapes that indicate the required C_L are obtained. Secondly, two types of airfoil data, that is, the NACA and the Joukowski airfoils, are used to obtain shapes that are different from both the NACA and Joukowski airfoils. \mathcal{S} -CVAE and the \mathcal{N} -CVAE model are used to perform these tasks.

The remainder of this paper is organized as follows. Section 2 introduces the CVAE model Section 3 describes the shape generation method. The proposed method is applied to the NACA airfoil data in Section 4. In Section 5, the proposed method is applied to a combination of the NACA and the Joukowski airfoils. Lastly, Section 6 concludes the paper.

2 Machine learning model

2.1 Conditional variational autoencoder

The CVAE is a neural network model, which is an extension of an AE and a VAE, as illustrated in Figure 1. The AE consists of an encoder and a decoder; the encoder extracts the features from the input data and the decoder reconstructs the data from these features. Essentially, the encoder reduces the dimension of the data. This feature is also known as a latent vector, and the space of the latent vector is called the latent space. The latent space in an AE is usually a Euclidean space, i.e., \mathbb{R}^d . An AE model is trained to output the same data as the input. The objective function of the training is to minimize the reconstruction loss, $\mathcal{L}_{\text{rec}} = \|\mathbf{x} - \mathbf{y}\|^2$, where \mathbf{x} and \mathbf{y} represent the input and the output vectors, respectively.

The VAE uses probability distribution in the latent space and the ordinal VAE uses a normal distribution in the Euclidean space; therefore, the ordinal VAE is represented as \mathcal{N} -VAE. The normal distribution is implemented using the equation, $\mathbf{x} = \boldsymbol{\mu} + \mathcal{N}_d(\mathbf{0}, I)\boldsymbol{\sigma}$, where $\mathcal{N}_d(\mathbf{0}, I)$ is a d -dimensional normal distribution with the variance-covariance matrix, I , $\boldsymbol{\mu} \in \mathbb{R}^d$ is a mean vector, $\boldsymbol{\sigma} \in \mathbb{R}^d$ is a variance vector, and I is an identity matrix. The VAE model is also trained to output the same data as the input, but its objective function differs from that of the AE. The objective function, \mathcal{L} , is the sum of the reconstruction loss and the KL divergence, $\mathcal{L}_{\text{KL}}(p||q)$.

$$\mathcal{L} = \mathcal{L}_{\text{rec}} + \mathcal{L}_{\text{KL}}(p||q). \quad (1)$$

The KL divergence measures the difference between the two probability distributions, p and q . In the VAE model, p is the distribution of the latent vector and q is the standard normal distribution.

In the CVAE model, a label node is added to the input of the encoder and the decoder of the VAE model. The same value is input at both the nodes when the model is trained. The encoder reduces the dimension of input data with label, c , and the decoder reconstructs the data with the information of the label, c . The objective function of the CVAE is identical to that of the VAE, Eq.(1).

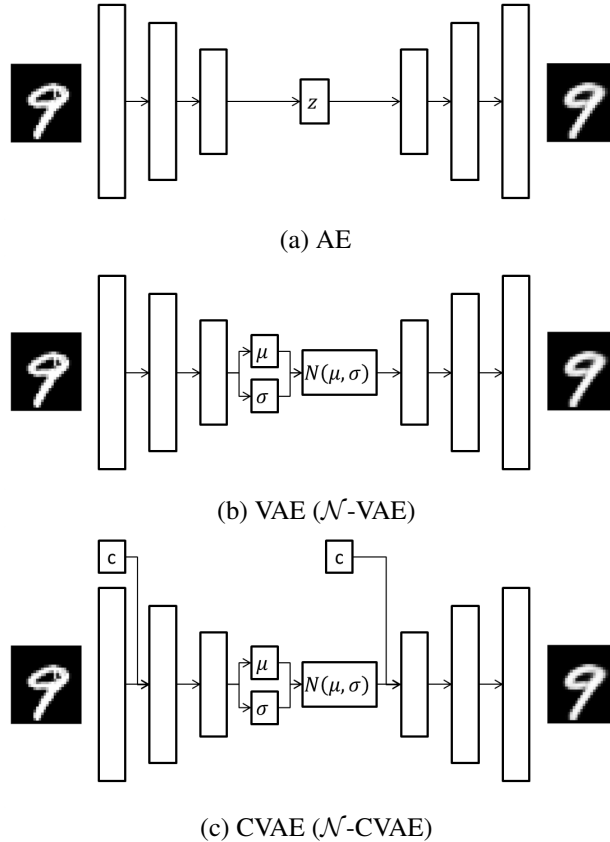


Figure 1: Schematics of AE, VAE, and CVAE.

2.2 Hyperspherical conditional variational autoencoder (\mathcal{S} -CVAE)

The Hyperspherical VAE has been proposed in [29]. In this study, the hyperspherical VAE is used for the CVAE, which is termed as the hyperspherical CVAE (\mathcal{S} -CVAE). The network architecture of the \mathcal{S} -VAE is nearly identical to that of the \mathcal{N} -VAE; the difference is that the \mathcal{S} -VAE uses a vMF distribution rather than a normal distribution. The probability density function of the vMF distribution is $f(x) = C \exp(\kappa \boldsymbol{\mu}^\top \mathbf{x})$, where the variable, \mathbf{x} , is defined as $\mathbf{x} \in \mathcal{S}$, $\mathcal{S} = \{\mathbf{x} \in \mathbb{R}^{d+1} \mid \|\mathbf{x}\| = 1\}$. $\boldsymbol{\mu} \in \mathcal{S}$ is the mean of the distribution, $\kappa \geq 0$ is a concentration parameter, and C is a constant term used to normalize the distribution. For a fixed $\boldsymbol{\mu}$, \mathbf{x} is concentrated at $\boldsymbol{\mu}$, and κ corresponds to the variance of the distribution. \mathcal{S} represents a d -dimensional hypersphere. Hence, the vMF distribution can be considered as a probability distribution in the hypersphere. The objective function of the \mathcal{S} -VAE is represented by Equation (1). The uniform distribution of the von Mises Fischer distribution, that is, $\text{vMF}(\cdot, 0)$, is used as the prior; $\text{vMF}(\boldsymbol{\mu}, \kappa)$ is used as the posterior. The KL divergence, \mathcal{L}_{KL} , is then calculated as follows:

$$\begin{aligned} \mathcal{L}_{KL}(\text{vMF}(\boldsymbol{\mu}, \kappa) \parallel \text{vMF}(\cdot, 0)) &= \kappa \frac{I_{d+1/2}(\kappa)}{I_{d+1/2-1}(\kappa)} + \left(\frac{d+1}{2} - 1 \right) \log \kappa - \frac{d+1}{2} \log(2\pi) \\ &\quad - \log I_{d+1/2-1}(\kappa) + \frac{d+1}{2} \log \pi + \log 2 - \log \Gamma \left(\frac{d+1}{2} \right) \end{aligned}$$

The KL divergence is a function of κ , but is independent of $\boldsymbol{\mu}$. This is because the prior is uniformly distributed on \mathcal{S} . Conversely, in a normal distribution, the prior is $\mathcal{N}(0, 1)$, because the mean of a normal distribution is located at the origin in a normal VAE, and the KL divergence is a function of $\boldsymbol{\mu}$.

One of the advantages of using the \mathcal{S} -VAE is avoiding the KL collapse. The KL collapse was reported in [30, 31] in the \mathcal{N} -VAE. The KL collapse is a situation in which the decoder outputs identical or similar data if a different latent vector is input. Davidson et al. [29] reported that the \mathcal{S} -VAE prevents the KL collapse, and outperforms the \mathcal{N} -VAE, especially when the input data has a circular structure.

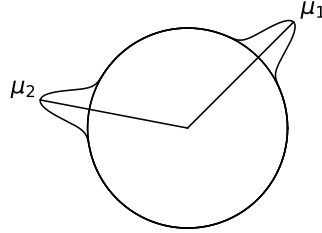


Figure 2: von Mises Fischer distribution $\text{vMF}(\boldsymbol{\mu}, \kappa = 100)$.

3 CVAE based shape generation method

3.1 Methodology

This study uses the CVAE model to analyze and generate shapes. The airfoil design task is shown in Figure 3. The machine learning model is trained once, and is used for multiple design queries. Once the model is trained, the model is re-used for many times. Both the \mathcal{N} -VAE and the \mathcal{S} -VAE are used in the numerical examples, with the same procedures for both models. The flowchart of the proposed method is presented in Figure 4. Initially, the dataset consists of the shape and its aerodynamic performance. In the numerical example, the airfoil shape data and its lift coefficient (C_L) are used.

The aim of this method is handle the different types of airfoils, that is, the NACA and the Joukowski airfoils. The shape is represented by using a set of points to handle the different types of shapes. If the free curves, e.g., Bézier curves, are used, the method of choosing the control points suitable for all the different types of shapes is not important. The outline of the airfoil is represented by a set of points, $(x_i, y_i)^\top$, and the shape is represented by $s = (x_1, x_2, \dots, x_n, y_1, y_2, \dots, y_n)^\top$. The lift coefficient is calculated by using Xfoil in Section 3.2, and the computation of Xfoil requires more than 120 points [32]. The number of points, n , was set as 248 in the following numerical example.

The dataset is split into the training and the test data with a ratio of 9 : 1. The training data are used to train the model, whereas the test data are used to evaluate the extent to which the trained model can reconstruct the unseen data. The

shapes, $\boldsymbol{\mu} = \frac{1}{|\mathcal{G}|} \sum_{\mathbf{x}_i \in \mathcal{G}} \mathbf{x}_i$ is then calculated, and the variation in the shape, v is calculated as the mean of the norm of the shape deviation. $v = \frac{1}{|\mathcal{G}|} \sum_{\mathbf{x}_i \in \mathcal{G}} \|\mathbf{x}_i - \boldsymbol{\mu}\|$.

3.2 DataSet

3.2.1 NACA airfoils

The NACA 4-digit airfoils are used in this study [33]. The total number of data points is 3696. The lift coefficient C_L is calculated by using the XFOil [32], which is a flow calculation toolbox based on the panel method. The distribution of C_L , shown in Figure 5 (a), is similar to a uniform distribution. The mean of the distribution is $\mu_{C_L} = 0.6866$, and the standard deviation is $\sigma_{C_L} = 0.3848$. An example of an NACA airfoil is shown in Figure 6 (a).

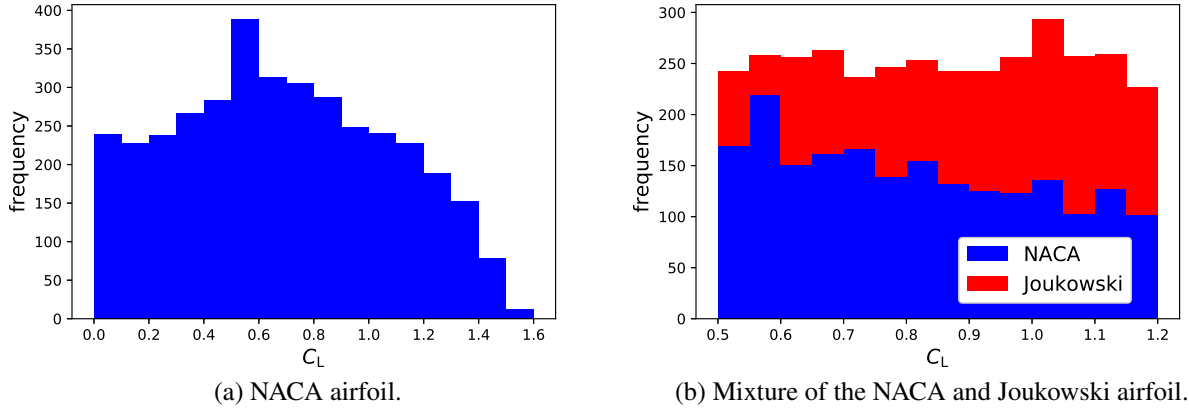


Figure 5: Histogram of C_L .

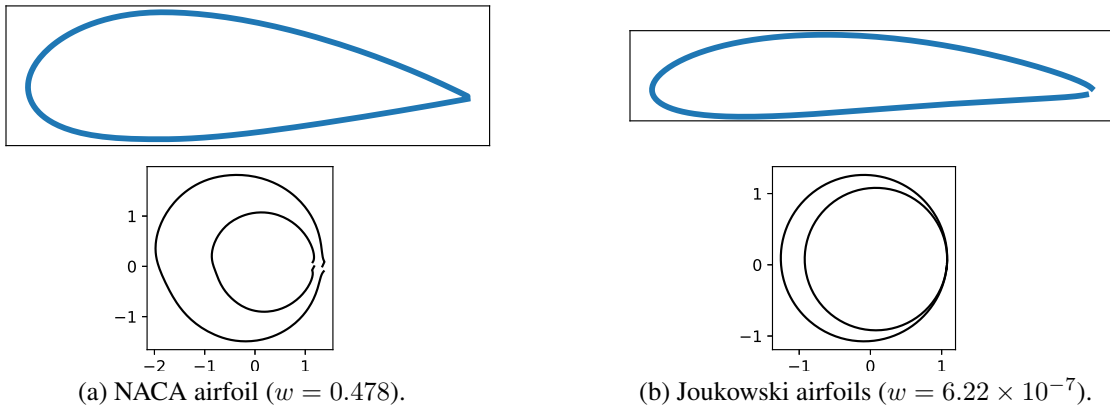


Figure 6: Examples of airfoils and Joukowski inverse transformation.

3.2.2 Joukowski airfoils

The Joukowski airfoil is a series of airfoils proposed by Joukowski. A set of points representing an airfoil shape, $\zeta \in \mathbb{C}$ is generated by the Joukowski transformation of a circle $z \in \mathbb{C}$. The Joukowski transformation is defined as follows:

$$\zeta = z + \frac{c_J^2}{z}, \quad (2)$$

where z is a circle and c_J is a variable defined by

$$\begin{aligned} |z - (a + bi)| &= r, \\ (c_J - a)^2 &= r^2 - b^2. \end{aligned}$$

where $a, b, c_J \in \mathbb{R}$. Various types of airfoils can be generated by changing $a, b, r, ..$. The parameters from $a \in \{0, 0.002, \dots, 0.2\}$, and $b \in \{0, 0.001, \dots, 0.2\}$ are chosen, and r is fixed at 1.1.

The generated shape, ζ is scaled such that its chord length becomes 1.0.

$$\text{Re}(\hat{\zeta}) = \frac{\text{Re}(\zeta) - \ell}{m}, \quad \text{Im}(\hat{\zeta}) = \frac{\text{Im}(\zeta)}{m}. \quad (3)$$

C_L is calculated in the same manner as the NACA airfoils. In this study, a dataset of the NACA airfoil and the Joukowski airfoil is constructed. The histogram of C_L of the NACA and the Joukowski airfoils is shown in Figure 5 (b). An example of the Joukowski airfoil is shown in Figure 6 (b).

The Joukowski airfoil is transformed into two circles by using the Joukowski inverse transformation. The mathematical formulation of the Joukowski inverse transformation is presented in Section A.1. If the Joukowski inverse transformation is applied to the NACA airfoil, the result is not a circle. Hence, by calculating the roundness of the inverse transformation, it can be determined whether the shape is similar to a Joukowski airfoil or not. Examples of the Joukowski inverse transformation to the NACA and the Joukowski airfoils are shown in Figure 6 (a) and (b), with the roundness, w . The value of w of the NACA airfoil is not zero, whereas the w of the Joukowski airfoil is sufficiently small.

4 NACA airfoil generation using \mathcal{S} -CVAE and \mathcal{N} -CVAE

In this section, the \mathcal{S} -CVAE and the \mathcal{N} -CVAE models are trained by using the NACA airfoil data. The aim of this task is to generate a wide variety of shapes which meet the required C_L . The program is implemented in Python using Tensorflow [34]. The computation was conducted on Intel Core i5-10210U 1.6 GHz CPU with 8GB memory.

4.1 Training and shape generation

The NACA airfoil data is fed to both \mathcal{N} -CVAE and \mathcal{S} -CVAE and new airfoil shapes are generated. The model is trained by using the same NACA data presented in section 3.2. The data are split in the ratio of 9 : 1 and fed as the training and the test datasets, respectively. The number of nodes in each layer is $n_1 = 500$ and $n_2 = 500$, where n_1 is used for the first layer of the encoder and the second layer of the decoder, and n_2 is used for the second layer of the encoder and the 1st layer of the decoder. The latent dimension, d , is also determined by comparing $\mathcal{L}_{C_L}^{gen}$, which is listed in Table 1. $d = 2$ is chosen as it indicates the smallest $\mathcal{L}_{C_L}^{gen}$.

Table 1: $\mathcal{L}_{C_L}^{gen}$ comparison with respect to different latent dimensions.

Lat. dim.	2	4	8	16	32
\mathcal{S} -CVAE	0.03019	0.03736	0.07091	0.04014	0.02213
\mathcal{N} -CVAE	0.05172	0.05282	0.05949	0.07300	0.06565

Table 2: \mathcal{L}_{C_L} of reconstructed and generated shapes.

Case	Train ($\mathcal{L}_{C_L}^{train}$)	Test ($\mathcal{L}_{C_L}^{test}$)	Generated from Random z ($\mathcal{L}_{C_L}^{gen}$)
\mathcal{N} -CVAE	0.02364	0.05140	0.05172
\mathcal{S} -CVAE	0.02829	0.04842	0.01965

The accuracy of the reconstructed and the generated shapes of both \mathcal{S} -CVAE and \mathcal{N} -CVAE are evaluated. \mathcal{L}_{C_L} are shown in Table 2. \mathcal{N} -CVAE and \mathcal{S} -CVAE exhibit similar values corresponding to $\mathcal{L}_{C_L}^{train}$ and $\mathcal{L}_{C_L}^{test}$, and the error distributions shown in Figure 7 (a)–(d) are also similar.

The new shapes are then generated. In \mathcal{S} -CVAE, 30 latent vectors are randomly sampled from the entire latent space, that is, $\{z \mid \|z\| = 1, z \in \mathbb{R}^{d+1}\}$. In \mathcal{N} -CVAE, 30 latent vectors are sampled from the envelope of the latent

vectors corresponding to the training data, and $\{z \mid L_i \leq z_i \leq U_i\}$, where L_i and U_i are the minimum and the maximum values of the latent vectors corresponding to the training data. When $\mathcal{L}_{C_L}^{\text{gen}}$ is calculated, the labels are set as $\mathcal{C} = \{0.0, 0.016, \dots, 1.584\}$. The results are shown in random z in Table 2, and Figure 7 (e) and (f). $\mathcal{L}_{C_L}^{\text{gen}}$ in \mathcal{S} -CVAE is 0.01965, which is less than half of that of \mathcal{N} -CVAE (0.05172). The error distribution is wider in \mathcal{N} -CVAE than in \mathcal{S} -CVAE. Consequently, \mathcal{S} -CVAE generates shapes more accurately corresponding to C_L . In both the \mathcal{S} -CVAE and \mathcal{N} -CVAE models, the error of C_L is small when the label, c^l , is in the middle of its range, that is, $0.4 < c^l < 1.2$, and is relatively large for other c^l . Recalling the histogram of C_L in Figure 5, the number of data points is smaller in the range, $1.2 < C_L$. This data imbalance may cause a larger error in this range.

In order to evaluate the shape variation, the shapes with sufficiently small error are first selected. The latent vectors which satisfy $\mathcal{L}_{C_L} < 0.02$ are chosen from 30 latent vectors. The number of selected latent vectors is 23 in \mathcal{S} -CVAE and 6 in \mathcal{N} -CVAE. From these shapes, five samples, A, B, C, D, and E, are selected, as shown in Figure 9. Additionally, the error of C_L is shown in Figure 7 (g) and (h). Figure 9 shows that the \mathcal{S} -CVAE generates a wider variety of shapes. This is also verified by calculating v , as explained in section 3.1. The histogram of v is shown in Figure 8. The histogram indicates that the generated shapes of \mathcal{S} -CVAE demonstrate a wider variation than \mathcal{N} -CVAE. Consequently, \mathcal{S} -CVAE generates various types of shapes.

4.2 Data embedding in the latent space

The difference between the \mathcal{S} -CVAE and the \mathcal{N} -CVAE lies in the shape of the latent space and the KL divergence. In this section, the latent space is visualized and the difference between both the models is observed. In addition to the CVAE, the VAE model is also analyzed in this section for comparison. The architecture of the VAE model is nearly identical to that of the CVAE model, except that the label is not input into the model. The training data are fed into the encoder, and the mean latent vector z is plotted in Figure 10 – Figure 12 with a contour of C_L . In the \mathcal{N} -VAE model (Figure 10 (a)), all the latent vectors shrink to $z = (0, 0)$, which indicates the KL collapse. In this case, all the data are encoded into the same area, and the decoder can output only one type of shape even though the training data has multiple shapes. The KL collapse does not occur in the \mathcal{S} -CVAE model (Figure 11). The latent vectors are widely distributed on the hypersphere. The input of the VAE model is only a set of shapes, and does not include the information on C_L . However, C_L gradually changes in the latent space. This may be due to the strong relationship between the C_L and the airfoil geometry.

Additionally, the KL collapse does not occur in the \mathcal{N} -CVAE and the \mathcal{S} -CVAE models (Figure 10 (b) and Figure 12 (a) and (b), respectively) as well, as observed in Section 4.1. In the CVAE model, the input of the decoder includes the latent vector as well as the label, C_L . Hence, the decoder processes the three-dimensional data in this case. To visualize the three-dimensional space, z is plotted with the label, C_L in a specific range (Figure 10 (c) – (f) and Figure 12 (c) – (j)).

In both the \mathcal{N} - and \mathcal{S} -CVAE models, the latent vectors are embedded in a similar area, even if the range of C_L is changed. This explains why, in Section 4.1, when one latent point is set and C_L is changed, the decoder outputs the appropriate airfoils. Conversely, for example, if one point is selected in the latent space, where the training data are embedded around the point in $C_L < 0.4$ and are not embedded in $1.2 < C_L$, then the decoder may output the wired shapes from the point for $1.2 < C_L$.

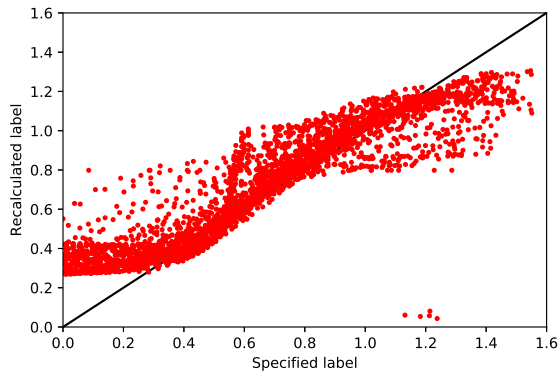
When \mathcal{N} - and \mathcal{S} -CVAE models are compared (Figure 10 (b) and Figure 12 (a) and (b)), the latent vectors are embedded in a narrower area in \mathcal{N} -CVAE when compared to \mathcal{S} -CVAE. As explained in the KL collapse in \mathcal{N} -VAE, if two training data are embedded in a very narrow area, the decoder cannot distinguish between these them, and outputs only one data even though the training data are different. \mathcal{S} -CVAE separates the training data and embeds it in a wider area. This difference in the latent space explains the difference in the shape variation in Section 4.1.

5 Combining the NACA and the Joukowski airfoils

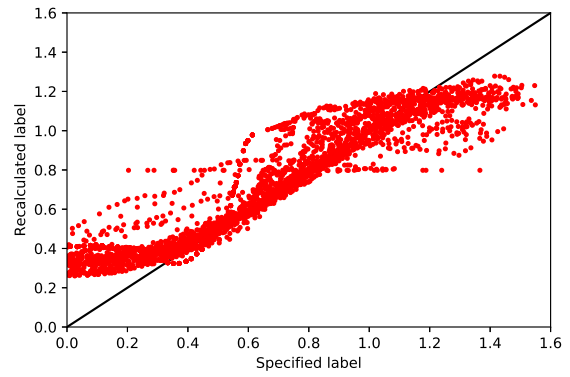
This section presents the utilization of the NACA and the Joukowski airfoil datasets. The aim is to generate novel shapes which are different from those of the NACA and the Joukowski airfoils.

5.1 Generated shapes

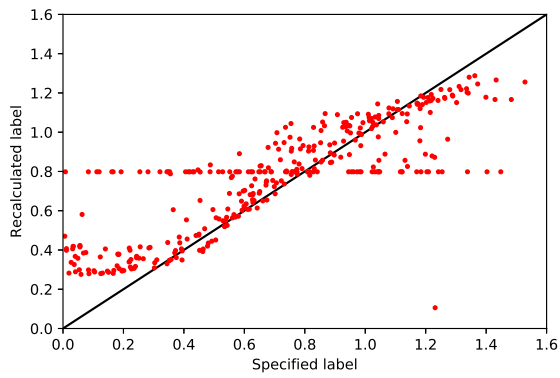
The NACA and the Joukowski datasets are combined into one dataset, and both the \mathcal{N} -CVAE and the \mathcal{S} -CVAE models are trained with a latent dimension of $d = 2$. The new shapes are then generated by using the random latent vectors. The label and the recalculated C_L of the generated shapes are plotted in Figure 13. The $\mathcal{L}_{C_L}^{\text{gen}}$ presents a nearly identical



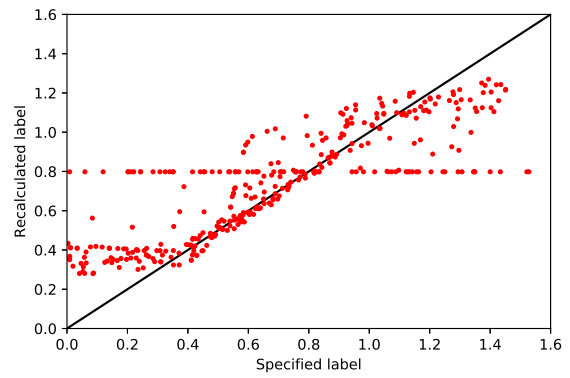
(a) Training data reconstruction using \mathcal{S} -CVAE.



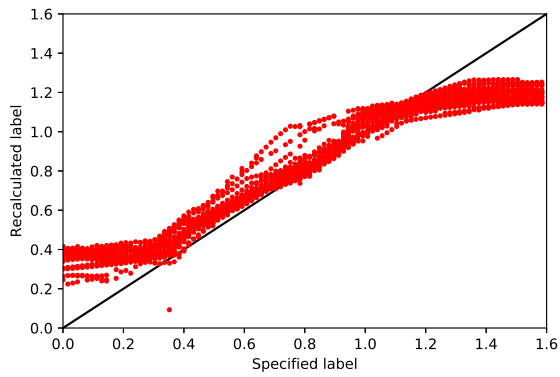
(b) Training data reconstruction using \mathcal{N} -CVAE.



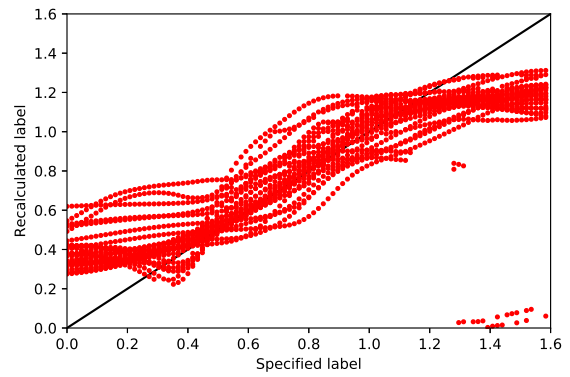
(c) Test data reconstruction using \mathcal{S} -CVAE.



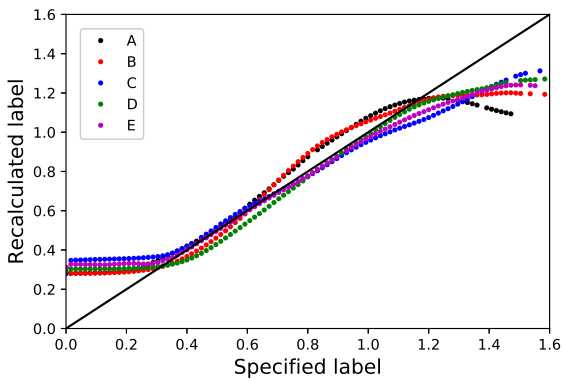
(d) Test data reconstruction using \mathcal{S} -CVAE.



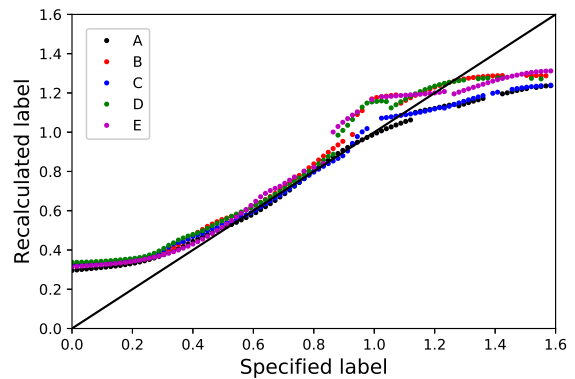
(e) Random sampling with \mathcal{S} -CVAE.



(f) Random sampling with \mathcal{N} -CVAE.



(g) Fixed latent sampling with \mathcal{S} -CVAE.



(h) Fixed latent sampling with \mathcal{N} -CVAE.

Figure 7: Error of C_L in generated airfoils.

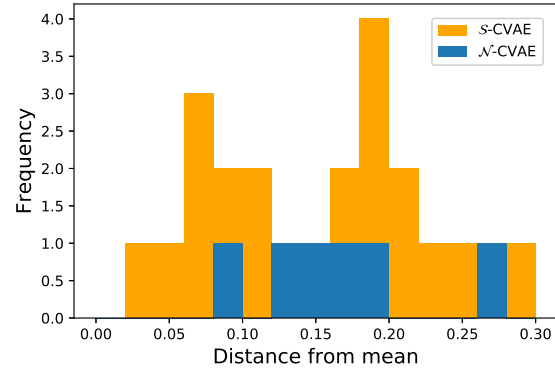


Figure 8: Histogram of shape variation v .



(a) S-CVAE.

(b) N-CVAE.

Figure 9: Generated shapes with $C_L = 0.687$.

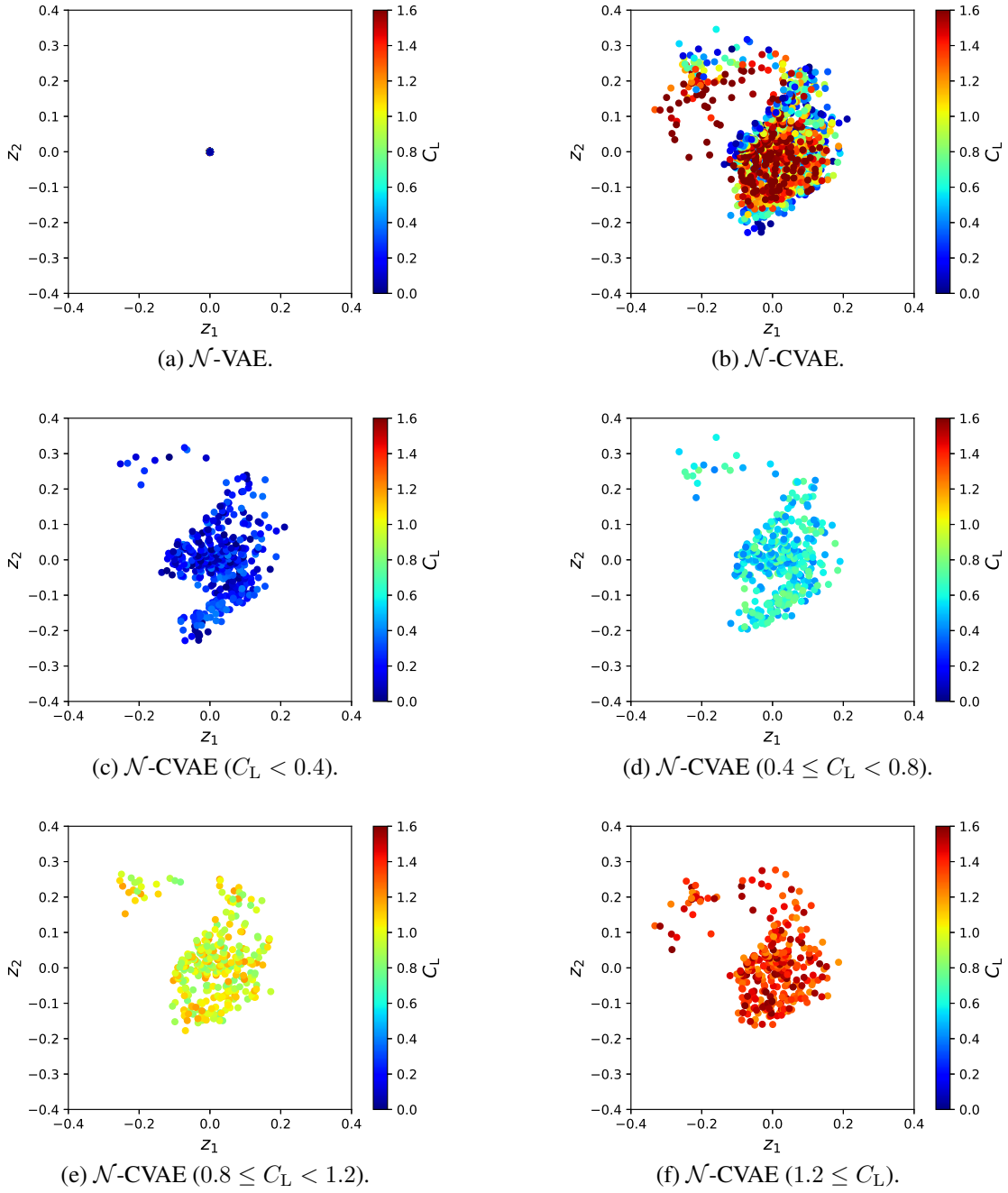


Figure 10: Latent map of \mathcal{N} -VAE and \mathcal{N} -CVAE with respect to C_L .

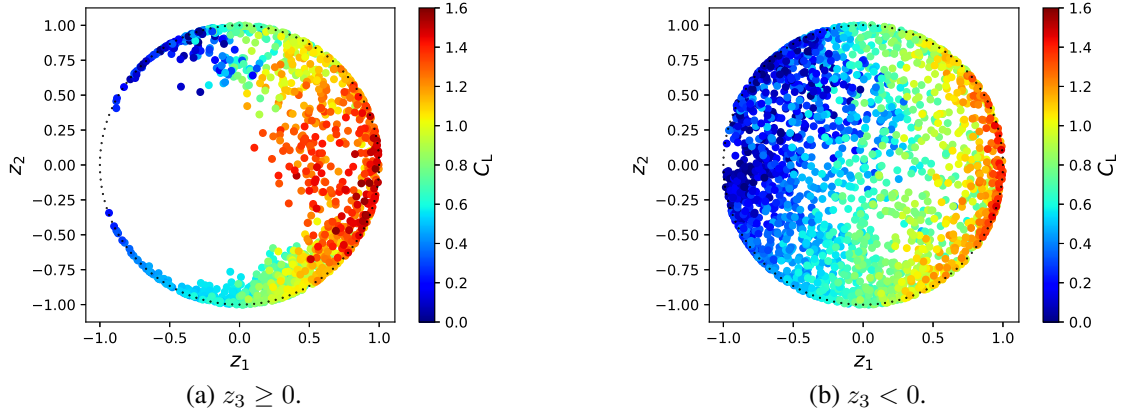


Figure 11: Latent map of \mathcal{S} -VAE with respect to C_L .

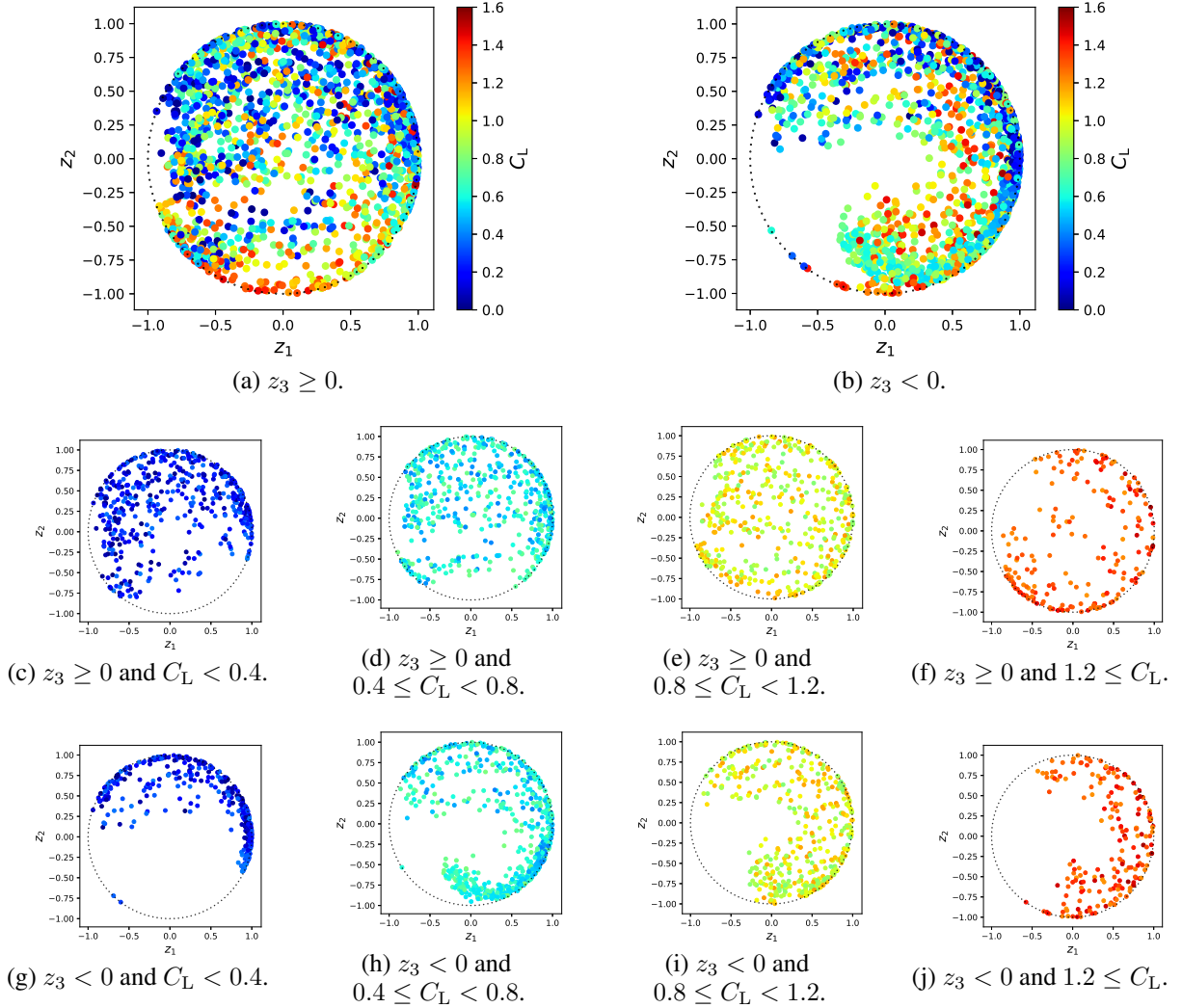


Figure 12: Latent map of \mathcal{S} -CVAE.

value in both the models. However, in the \mathcal{S} -CVAE model, the result is scattered more broadly when compared to the \mathcal{N} -CVAE.

The distance between each generated shape and the NACA and the Joukowski datasets are also calculated. Figure 14 (b) shows a sketch of the distance between a set of NACA airfoils and a set of Joukowski airfoils. The Euclidean distance between the two sets is 1.92. The histograms are shown in Figure 14. The histogram of both models indicates that their distribution is completely different. In \mathcal{S} -CVAE, the histogram has two peaks around 0.0 and 2.0, which indicates that the generated shapes are similar to those of the NACA and the Joukowski airfoils, respectively. Conversely, the distance in \mathcal{S} -CVAE, is distributed in the range of [0.5, 1.4]. This implies that the generated shapes are located in the middle of the NACA and the Joukowski airfoils as illustrated in Figure 14 (c). Consequently, the generated data in \mathcal{N} -CVAE are a combination of the NACA airfoils and the Joukowski airfoils.

The Joukowski inverse transformation is conducted on the generated shapes and the training data. The result is shown in Figure 15. The roundness, w , in the \mathcal{S} -CVAE model has a wide distribution, whereas \mathcal{N} -CVAE does not. Both the distance and the roundness results indicate that the variety of the generated shapes is large in \mathcal{S} -CVAE and small in \mathcal{N} -CVAE.

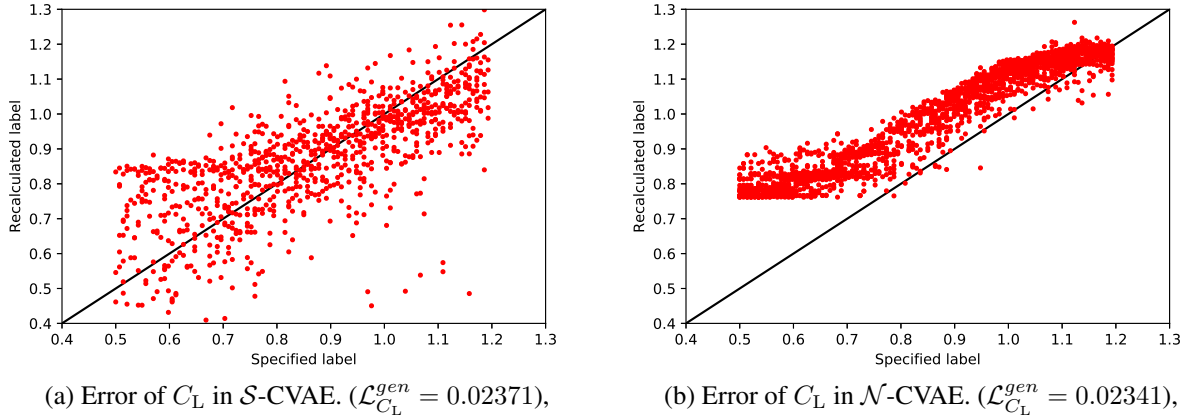


Figure 13: Comparison of error and $\mathcal{L}_{C_L}^{gen}$.

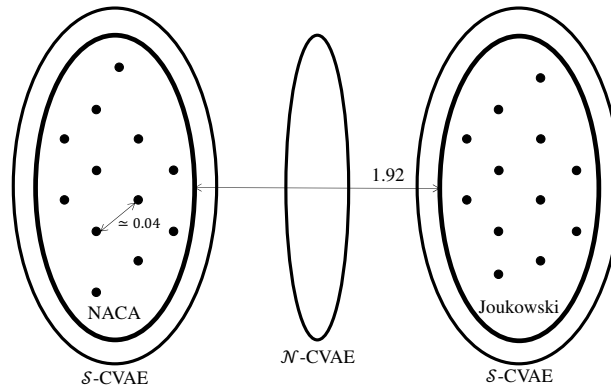
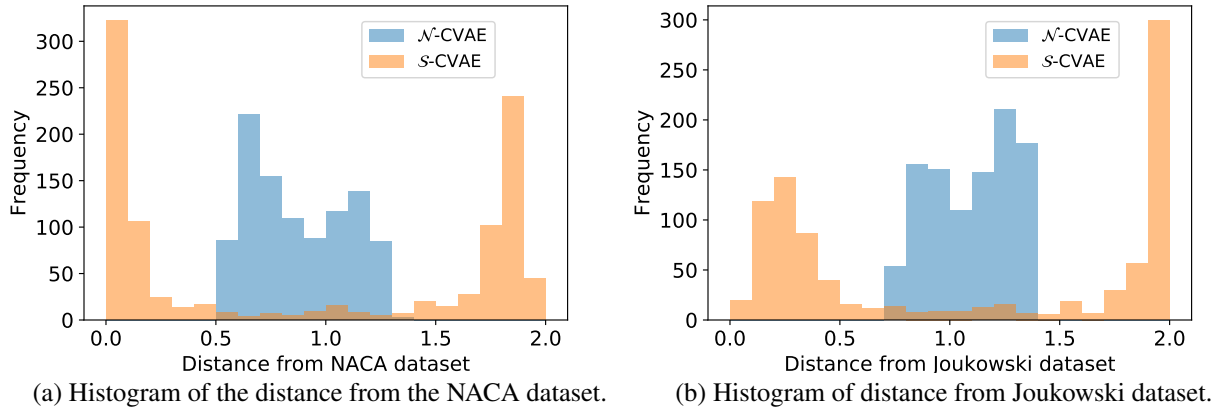
The distance between generated shapes and train data can be controlled by changing the ratio of NACA and Joukowski data. We multiply Joukowski data by three by duplicating data, and trained \mathcal{N} -CVAE model ($3 \times$ Joukowski case). The distance and w of the generated shapes are shown in Figure 16 and Figure 17. The generated shapes locate closer to Joukowski airfoils than Figure 14. w also indicates smaller value than Figure 17. These result implies that the generated shapes can be controlled by changing the ratio of the dataset.

5.2 Distribution in latent space

A plot of w in the latent space is shown in Figure 18 (a) and (b) and in Figure 19 (a). The points where the NACA and the Joukowski airfoils are embedded is shown in Figure 18 (c) and (d) and Figure 19 (b). In the \mathcal{S} -CVAE, the NACA airfoils and the Joukowski airfoils form clusters in the hypersphere. Conversely, in the \mathcal{N} -CVAE, the NACA and the Joukowski airfoils are combined. This difference corresponds to the capability of the \mathcal{S} -CVAE in the separation of the latent data, as observed in Section 4.

In \mathcal{S} -CVAE, the roundness, w , is relatively high (i.e., larger than 0.4) in the area where neither the NACA nor the Joukowski airfoils are embedded, and relatively low, that is, smaller than 0.1, in the area where the Joukowski airfoils are embedded. Conversely, w is randomly distributed in the latent space in \mathcal{N} -CVAE. The shapes generated from the latent vectors S1–S5 and N1–N2 are shown in Figure 20. The locations of the latent vectors are shown in Figure 18 and Figure 19. S1 and S2 indicate a small value of w because they are decoded from the Joukowski area, whereas S5 indicates a moderate value of w because it is decoded from the NACA area. Both cases produce appropriate airfoil shapes. However, S3 and S4 form wired shapes because they are decoded from the areas where no training data are embedded. Therefore, N1–N3 produce appropriate shapes.

Consequently, \mathcal{S} -CVAE is more capable of separating data, and hence it embeds the NACA and the Joukowski airfoils in separate areas. The generated shapes are also separated into two types: the NACA-like shapes and the Joukowski-like



(c) Sketch of distance between training data.

Figure 14: Distance between generated shapes and train data.

shapes. However, the \mathcal{N} -CVAE lacks the capability of data separation. Therefore, \mathcal{N} -CVAE embeds both the NACA and the Joukowski airfoils in the same area in the latent space, due to which, the decoder must generate intermediate shapes between the NACA and the Joukowski shapes.

6 Conclusion

This study proposed the CVAE based method to generate a variety of shapes. Two types of CVAE models, namely, the \mathcal{S} -CVAE and the \mathcal{N} -CVAE models, were analyzed to train and generate the airfoil data. Two tasks were set for this analysis. The first task involves the training and the generation of the NACA airfoil data. The main objective is to generate a wide variety of NACA-like airfoils. The other task is to use the NACA and the Joukowski airfoils for the training and generation of novel shapes which are different from both the NACA and the Joukowski airfoils.

The \mathcal{S} -CVAE model is superior to the \mathcal{N} -CVAE models when applied to single type of airfoil, as it separates the data in the latent space. However, if different types of data are to be combined, for example, the NACA airfoil and the Joukowski airfoil, \mathcal{S} -CVAE outputs only the NACA-like airfoils and the Joukowski-like airfoils, and does not output the feature-mixed airfoils. The generated shapes are nearly identical to the training data and are not novel shapes.

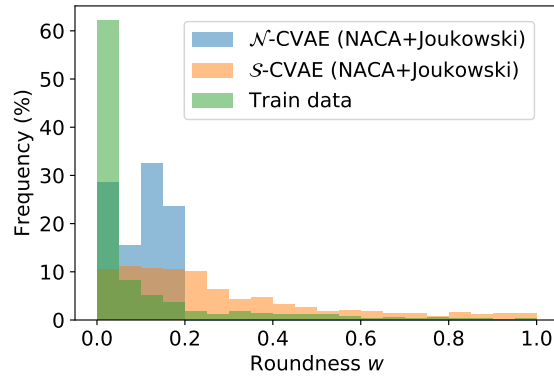


Figure 15: Histogram of roundness in Joukowski inverse transformation.

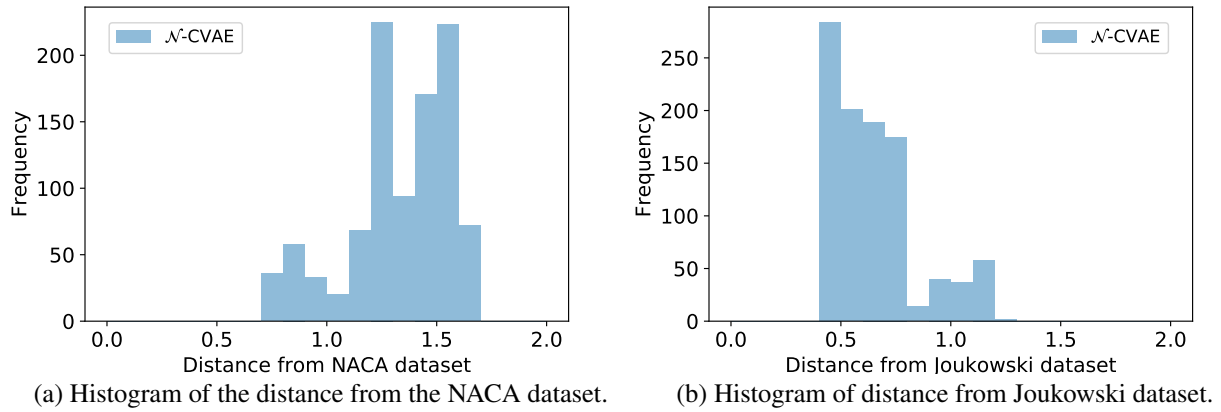


Figure 16: Distance between generated shapes and train data ($3 \times$ Joukowski case).

Conversely, the \mathcal{N} -CVAE model combines different features and generates novel shapes. This is due to the lack of the data separation capability.

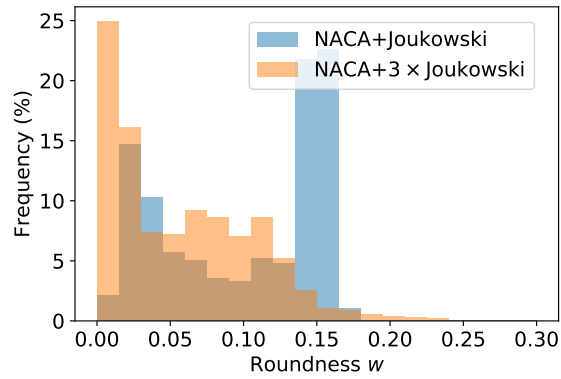


Figure 17: Histogram of roundness in Joukowski inverse transformation ($3 \times$ Joukowski case).

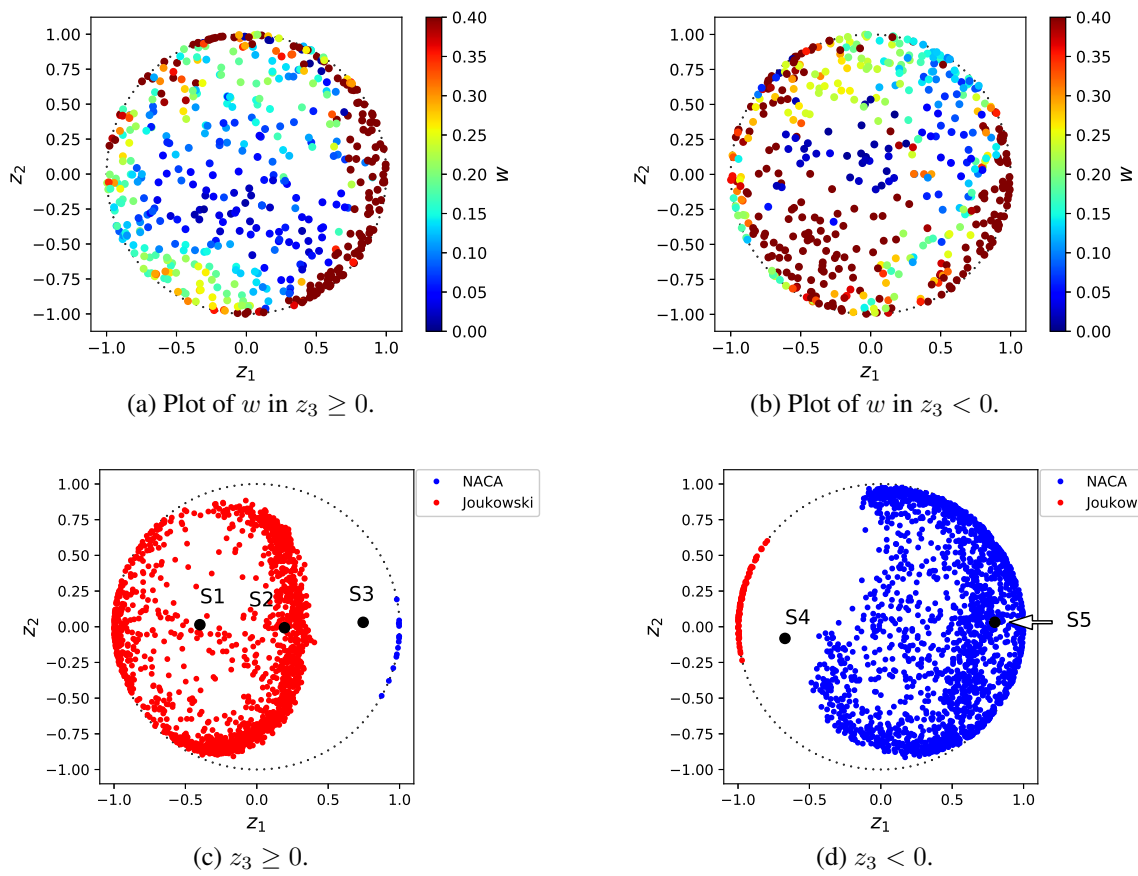


Figure 18: Plot of w and embedded airfoil types (\mathcal{S} -CVAE).

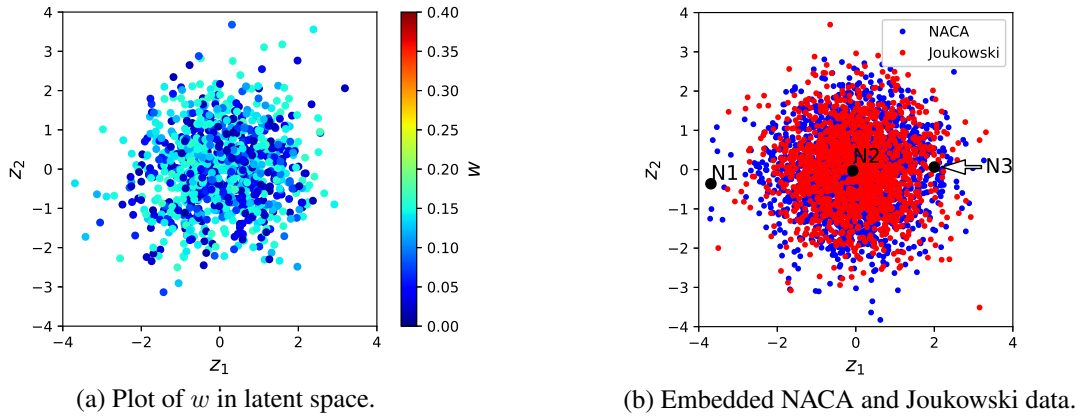


Figure 19: Plot of w and embedded airfoil types (\mathcal{N} -CVAE).

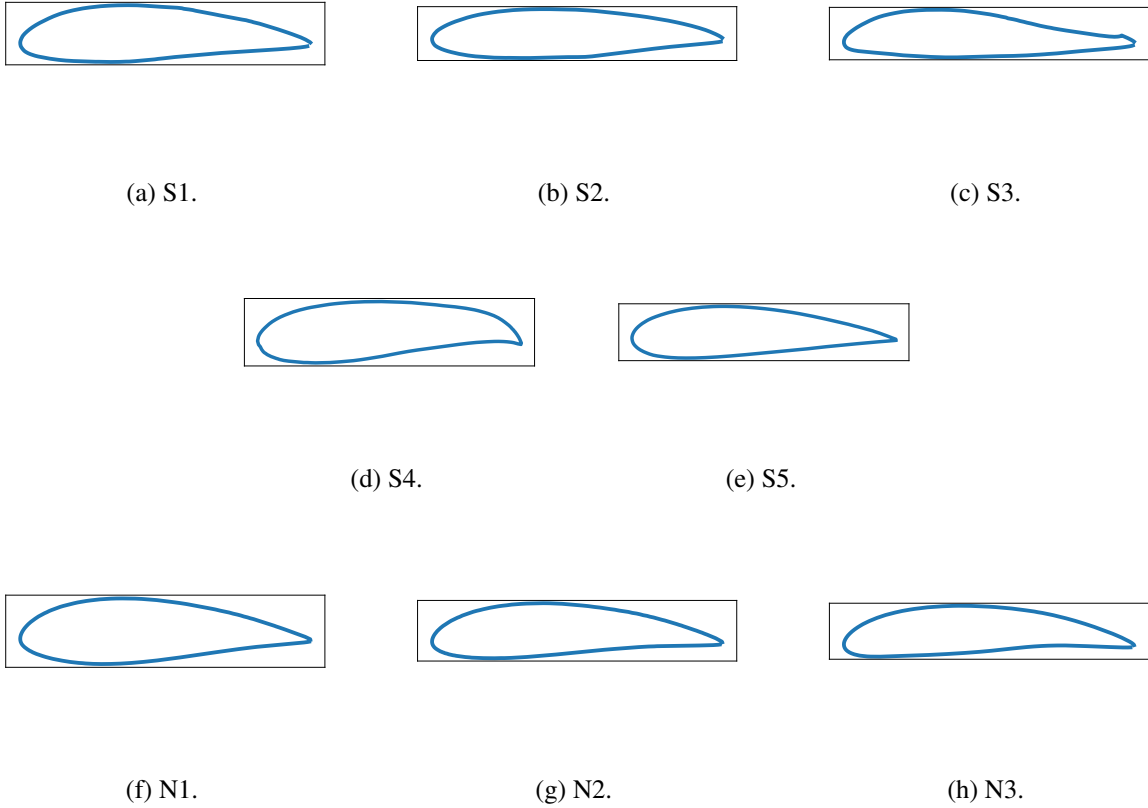


Figure 20: Generated shapes from different latent vectors.

A.1 Joukowski inverse transformation

In this section, a Joukowski inverse transformation of the given airfoil shape, $\widehat{\zeta}$. The generated shapes by CVAE model is normalized by (3). Hence, at first the shape is de-normalized as

$$\operatorname{Re}(\zeta) = \operatorname{Re}(\widehat{\zeta})m + \ell, \quad \operatorname{Im}(\zeta) = \operatorname{Im}(\widehat{\zeta})m$$

The Joukowski inverse transformation is derived from Equation (2) as

$$\begin{aligned} \zeta = z + \frac{c_J^2}{z} &\Leftrightarrow z^2 - \zeta z + c_J^2 = 0 \\ &\Leftrightarrow z = \frac{1}{2}(\zeta \pm \sqrt{\zeta^2 - 4c_J}). \end{aligned} \quad (4)$$

In equation (4), c_J is a function of a , b , and r , and cannot be determined from ζ . Additionally, the scale factors, ℓ and m , in (3) are unknown. Hence, c_J , ℓ , and m , which define the most suitable inverse transformation, are searched.

For a given set of points, z_i ($i = 1, \dots, N$), the inverse transformation yields a set of points, ζ_i . If the appropriate c_J , ℓ , and m , are chosen, ζ_i forms two circles. The Joukowski transformation generates the same airfoil from both the circles. However, if c_J , ℓ , and m , ζ_i are not appropriately chosen, z_i does not form the circles. Hence, c_J , ℓ , and m are optimized by minimizing the mean squared error from a circle denoted by ω . From x_i and y_i , which are the real and imaginary parts of z_i , that is, $z_i = x_i + iy_i$, ω is defined by

$$\begin{aligned} \omega &= \sum_i \left((x_i - a)^2 + (y_i - b)^2 - r^2 \right)^2 \\ &= \sum_i (x_i^2 + y_i^2 + Ax_i + By_i + C), \end{aligned} \quad (5)$$

where a and b are the centers of the circles, and $r = 1.1$ is the radius defined in Section 3.2.2, $A = -2a$, $B = -2b$, and $C = a^2 + b^2 - r^2$. Because Ω is a convex function with respect to a , b , and r , the global optimal solution can be obtained by solving the stationary condition, $\frac{\partial \omega}{\partial A} = 2x_i\omega$, $\frac{\partial \omega}{\partial B} = 2y_i\omega$, $\frac{\partial \omega}{\partial C} = 2\omega$. A , B , and C are calculated from the stationary conditions as:

$$\begin{pmatrix} A \\ B \\ C \end{pmatrix} = \begin{pmatrix} \sum_i x_i^2 & \sum_i x_i y_i & \sum_i x_i \\ \sum_i x_i y_i & \sum_i y_i^2 & \sum_i y_i \\ \sum_i x_i & \sum_i y_i & n \end{pmatrix}^{-1} \begin{pmatrix} -\sum_i (x_i^3 - x_i y_i^2) \\ -\sum_i (x_i^2 y_i - y_i^3) \\ -\sum_i (x_i^2 - y_i^2) \end{pmatrix}.$$

Therefore, ω is calculated from z and the calculation is denoted as $\omega = f(z)$.

The parameters, c_J , ℓ , and m which minimize ω are located. The optimization problem is given as:

$$\begin{aligned} &\text{given} && \widehat{\zeta} \\ &\text{minimize}_{c_J, \ell, m}, && \omega = f(z), \\ &\text{such that} && \operatorname{Re}(\zeta_i) = \operatorname{Re}(\widehat{\zeta}_i)m + \ell, \\ & && \operatorname{Im}(\zeta_i) = \operatorname{Im}(\widehat{\zeta}_i)m, \\ & && z_i = \frac{1}{2} \left(\zeta_i \pm \sqrt{\zeta_i^2 - 4c_J} \right). \end{aligned}$$

w is the minimum mean squared error of the inverse-transformed shapes from any circle. Hence, w is equivalent to roundness of the inverse-transformed shapes.

References

- [1] Duccio Bonaiuti, Mehrdad Zangeneh, Reima Aartotarjari, and Jonas Eriksson. Parametric design of a waterjet pump by means of inverse design, cfd calculations and experimental analyses. *Journal of Fluids Engineering*, 132(3):031104, 2010.
- [2] Akira Goto and Mehrdad Zangeneh. Hydrodynamic design of pump diffuser using inverse design method and cfd. *Journal of Fluids Engineering*, 124(2):319–328, 2002.

- [3] Stephen R. Kennon and George S. Dulikravich. Inverse Design of Coolant Flow Passage Shapes With Partially Fixed Internal Geometries. volume Volume 3: Heat Transfer; Electric Power of *Turbo Expo: Power for Land, Sea, and Air*, 03 1985. V003T09A016.
- [4] Shuliang Cao, Guoyi Peng, and Zhiyi Yu. Hydrodynamic design of rotodynamic pump impeller for multiphase pumping by combined approach of inverse design and cfd analysis. *Journal of Fluids Engineering*, 172(2):330–338, 2005.
- [5] Wang Zhengming. Inverse Design Calculations for Transonic Cascades. *Turbo Expo: Power for Land, Sea, and Air*, 03 1985. V001T03A005.
- [6] R. Narducci, B. Grossman, and R. T. Haftka. Sensitivity algorithms for an inverse design problem involving a shock wave. *Inverse Problems in Engineering*, 2(1):49–83, 1995.
- [7] D. A. Tortorelli and P. Michaleris. Design sensitivity analysis: Overview and review. *Inverse Problems in Engineering*, 1(1):71–105, 1994.
- [8] Kazuo Yonekura and Osamu Watanabe. A shape parameterization method using principal component analysis in application to shape optimization. *Journal of Mechanical Design*, 136:121401, 2014.
- [9] Stefano Gaggero, Giuliano Vernengo, Diego Villa, and Luca Bonfiglio. A reduced order approach for optimal design of efficient marine propellers. *Ships and Offshore Structures*, 0(0):1–15, 2019.
- [10] T. Bui-Thanh, M. Damodaran, and K. Willcox. Aerodynamic Data Reconstruction and Inverse Design Using Proper Orthogonal Decomposition. *AIAA Journal*, 42(8):1505–1516, 2004.
- [11] Ikjin Lee, K.K. Choi, and David Gorsick. System reliability-based design optimization using the MPP-based dimension reduction method. *Computer Methods in Applied Mechanics and Engineering*, 41(6):823–839, 2010.
- [12] Nathan C Brown and Caitlin T Mueller. Design variable analysis and generation for performance-based parametric modeling in architecture. *International Journal of Architectural Computing*, 17(1):36–52, 2019.
- [13] Kozo Nita, Yoji Okita, Chiyuki Nakamata, Seiji Kubo, Kazuo Yonekura, and Osamu Watanabe. Film cooling hole shape optimization using proper orthogonal decomposition. *ASME Turbo Expo 2014: Turbine Technical Conference and Exposition*, 2014. GT2014-27239.
- [14] Kozo Nita, Yoji Okita, Chiyuki Nakamata, Seiji Kubo, Kazuo Yonekura, and Osamu Watanabe. Turbine blade, 2017. US Patent 9,759,069.
- [15] Gabriel Achour, Woong Je Sung, Olivia J. Pinon-Fischer, and Dimitri N. Mavris. *Development of a Conditional Generative Adversarial Network for Airfoil Shape Optimization*, page 2261.
- [16] Wei Chen, Kevin Chiu, and Mark Fuge. BézierGAN: Automatic generation of smooth curves from interpretable low-dimensional parameters. *arXiv*, 2021. 1808.08871v2.
- [17] Xiang Li, Shaowu Ning, Zhanli Liu, Ziming Yan, Chengcheng Luo, and Zhuo Zhuang. Designing phononic crystal with anticipated band gap through a deep learning based data-driven method. *Structural and Multidisciplinary Optimization*, 361:112737, 2020.
- [18] Kazuo Yonekura and Hitoshi Hattori. Framework for design optimization using deep reinforcement learning. *Structural and Multidisciplinary Optimization*, 60(4):1709–1713, 2019.
- [19] Yonggyun Yu, Taeil Hur, Jaeho Jung, and In Gwon Jang. Deep learning for determining a near-optimal topological design without any iteration. *Structural and Multidisciplinary Optimization*, 59(3):787–799, 2019.
- [20] Ren Kai Tan, Nevin L. Zhang, and Wenjing Ye. A deep learning-based method for the design of microstructural materials. *Structural and Multidisciplinary Optimization*, 61(4):1417–1438, 2020.
- [21] Yujie Zhang and Wenjing Ye. Deep learning-based inverse method for layout design. *Structural and Multidisciplinary Optimization*, 60(2):527–536, 2019.
- [22] Geoffrey Hinton and Ruslan R. Salakhutdinov. Reducing the dimensionality of data with neural networks. *Science*, 313(5786):504–507, 2006.
- [23] Diederik P. Kingma and Max Welling. Auto-encoding variational bayes. *arXiv*. 1312.6114.
- [24] Yunchen Pu, Zhe Gan, Ricardo Henao, Xin Yuan, Chunyuan Li, Andrew Stevens, and Lawrence Carin. Variational autoencoder for deep learning of images, labels and captions. In D. D. Lee, M. Sugiyama, U. V. Luxburg, I. Guyon, and R. Garnett, editors, *Advances in Neural Information Processing Systems 29*, pages 2352–2360. Curran Associates, Inc., 2016.

- [25] Haowen Xu, Wenxiao Chen, Nengwen Zhao, Zeyan Li, Jiahao Bu, Zhihan Li, Ying Liu, Youjian Zhao, Dan Pei, Yang Feng, Jie Chen, Zhaogang Wang, and Honglin Qiao. Unsupervised anomaly detection via variational auto-encoder for seasonal kpis in web applications. In *Proceedings of the 2018 World Wide Web Conference, WWW'18*, pages 187–196. International World Wide Web Conferences Steering Committee, 2018.
- [26] K. Sohn, H. Lee, and X. Yan. Learning structured output representation using deep conditional generative models. In *Advances in Neural Information Processing Systems 28*, pages 3483–3491, 2015.
- [27] Ilya Tolstikhin, Olivier Bousquet, Sylvain Gelly, and Bernhard Schoelkopf. Wasserstein auto-encoders. *arXiv*. 1711.01558.
- [28] Md. Abul Hasnat, Julien Bohne, Jonathan Milgram, Stephane Gentric, and Liming Chen. von Mises-Fisher mixture model-based deep learning: Application to face verification. *arXiv*. 1706.04264v2.
- [29] Tim R. Davidson, Luca Falorsi, Nicola De Cao, Thomas Kipf, and Jakub M. Tomczak. Hyperspherical variational auto-encoders. *34th Conference on Uncertainty in Artificial Intelligence (UAI-18)*, 2018.
- [30] T. Song, J. Sun, B. Chen, W. Peng, and J. Song. Latent space expanded variational autoencoder for sentence generation. *IEEE Access*, 7:144618–144627, 2019.
- [31] Y. Zhang, S. Pan, L. He, and Z. Ling. Learning latent representations for style control and transfer in end-to-end speech synthesis. In *ICASSP 2019 - 2019 IEEE International Conference on Acoustics, Speech and Signal Processing (ICASSP)*, pages 6945–6949, 2019.
- [32] Mark Drela. Xfoil: An analysis and design system for low Reynolds number airfoils. In Mueller T.J., editor, *Low Reynolds Number Aerodynamics*, volume 54 of *Lecture Notes in Engineering*, pages 1–12. Springer, Berlin, Heidelberg, 1989.
- [33] Ira H. Abbot, Albert E. von Doenhoff, and Louis Stivers, Jr. *Summary of Airfoil Data*. United States, 1945.
- [34] Martín Abadi, Ashish Agarwal, Paul Barham, Eugene Brevdo, Zhifeng Chen, Craig Citro, Greg S. Corrado, Andy Davis, Jeffrey Dean, Matthieu Devin, Sanjay Ghemawat, Ian Goodfellow, Andrew Harp, Geoffrey Irving, Michael Isard, Yangqing Jia, Rafal Jozefowicz, Lukasz Kaiser, Manjunath Kudlur, Josh Levenberg, Dandelion Mané, Rajat Monga, Sherry Moore, Derek Murray, Chris Olah, Mike Schuster, Jonathon Shlens, Benoit Steiner, Ilya Sutskever, Kunal Talwar, Paul Tucker, Vincent Vanhoucke, Vijay Vasudevan, Fernanda Viégas, Oriol Vinyals, Pete Warden, Martin Wattenberg, Martin Wicke, Yuan Yu, and Xiaoqiang Zheng. TensorFlow: Large-scale machine learning on heterogeneous systems, 2015. Software available from tensorflow.org.